



Cite this: *J. Mater. Chem. A*, 2015, 3, 10378

## Scalable synthesis of $\text{Na}_3\text{V}_2(\text{PO}_4)_3/\text{C}$ porous hollow spheres as a cathode for Na-ion batteries

Jianfeng Mao, Chao Luo, Tao Gao, Xiulin Fan and Chunsheng Wang\*

$\text{Na}_3\text{V}_2(\text{PO}_4)_3$  (NVP) has been considered as a very promising cathode material for sodium-ion batteries (SIBs) due to its typical NASICON structure, which provides an open and three dimensional (3D) framework for  $\text{Na}^+$  migration. However, the low electronic conductivity of NVP limits its rate capability and cycling ability. In this study, carbon coated hollow structured NVP/C composites are synthesized via a template-free and scalable ultrasonic spray pyrolysis process, where the carbon coated NVP particles are uniformly decorated on the inner and outer surfaces of the porous hollow carbon spheres. When evaluated as a cathode material for SIBs, the unique NVP/C porous hollow sphere cathode delivers an initial discharge capacity of  $99.2 \text{ mA h g}^{-1}$  and retains  $89.3 \text{ mA h g}^{-1}$  after 300 charge/discharge cycles with a very low degradation rate of 0.035% per cycle. For comparison, the NVP/C composite, prepared by the traditional sol-gel method, delivers a lower initial discharge capacity of  $97.4 \text{ mA h g}^{-1}$  and decreases significantly to  $71.5 \text{ mA h g}^{-1}$  after 300 cycles. The superior electrochemical performance of NVP/C porous hollow spheres is attributed to their unique porous, hollow and spherical structures, as well as the carbon-coating layer, which provides a high contact area between electrode/electrolyte, high electronic conductivity, and high mechanical strength.

Received 6th February 2015

Accepted 2nd April 2015

DOI: 10.1039/c5ta01007a

www.rsc.org/MaterialsA

## Introduction

Lithium-ion batteries (LIBs) have become the most successful energy storage sources for portable electronic devices since their first commercialization in 1991. Nowadays, LIBs are also considered as potential energy storage devices for electric vehicles/hybrid electric vehicles (EVs/HEVs) and large-scale renewable energy storage systems (ESS).<sup>1</sup> However, recent concerns on the availability of lithium have led to strong interest in sodium-ion batteries (SIBs).<sup>2–5</sup> Sodium is one of the most abundant elements in the Earth (2.64 wt% in the Earth), and sodium resources are inexpensive and unlimited in rock and seas. Considering the material abundance and cost, SIBs are an ideal alternative to LIBs, especially for application in large-scale energy storage.<sup>2</sup> More importantly, sodium has similar chemical properties to lithium, which makes knowledge of developing LIBs valuable for the design of SIB electrodes.<sup>3</sup>

However, challenges still remain since there are several fundamental differences between SIBs and LIBs. First, the ionic radius of  $\text{Na}^+$  is larger than  $\text{Li}^+$  (0.98 Å vs. 0.69 Å).<sup>4</sup> The larger  $\text{Na}^+$  ions will lead to slower ion transport, more sluggish reaction kinetics and larger volume change upon  $\text{Na}^+/\text{Na}$  insertion/extraction, which usually result in limited rate capability and Na storing reversibility.<sup>5</sup> Second, the general preference for octahedral or prismatic coordination has limited the structure

options of Na insertion electrodes.<sup>6</sup> Therefore, electrode materials with large interstitial space to accommodate the volume expansion caused by rapid Na-ion insertion are highly recommended.<sup>3–5</sup>

Recently, many cathode materials such as layered transition sodium oxides  $\text{Na}_x\text{MO}_{2+y}$  ( $\text{M} = \text{Mn}, \text{Co}, \text{Fe}, \text{etc.}$ ),<sup>7–10</sup> olivine  $\text{NaMPO}_4$  ( $\text{M} = \text{Fe}, \text{Mn}, \text{etc.}$ ),<sup>11–13</sup> sulfates ( $\text{NaFeSO}_4\text{F}$ ,  $\text{Na}_2\text{Fe}_2(\text{SO}_4)_3$ , *etc.*),<sup>14,15</sup> and sodium super ionic conductors (NASICON)  $\text{Na}_x\text{M}_2(\text{PO}_4)_3$  ( $\text{M} = \text{Ti}, \text{V}, \text{etc.}$ )<sup>16,17</sup> have been investigated. Among various cathode materials for SIBs, sodium vanadium(III) phosphate ( $\text{Na}_3\text{V}_2(\text{PO}_4)_3$ , NVP) has attracted extensive attention due to its unique NASICON structure with a 3D network, which possesses large interstitial spaces and is able to facilitate  $\text{Na}^+$  transport. The NVP material also exhibits high Na-ion conductivity, high potential plateau (3.4 V), good specific capacity ( $117.6 \text{ mA h g}^{-1}$ , presuming two  $\text{V}^{3+}$  are oxidized to  $\text{V}^{4+}$ ), and high thermal stability. However, its low electric conductivity limits the electrochemical performance.<sup>18–21</sup>

Recent progress combining the designing of nanomaterials with optimized structures, and composite components by coating conductive carbon layers, or forming composites with conductive materials such as graphene, carbon nanofibers, or carbon nanotubes has greatly improved the electrochemical performance.<sup>22–42</sup> Considerable research efforts have been devoted to the fabrication of carbon coated NVP materials, in which both the solid state reaction and the sol-gel method can be applied in large-scale production. However, the poor electrochemical performances of these NVP/C composites synthesized

Department of Chemical and Biomolecular Engineering, University of Maryland, College Park, Maryland 20742, USA. E-mail: cswang@umd.edu

with those scalable methods cannot satisfy the requirement for high energy density and long cycle life of SIB cathodes. For example, the solid state synthesized NVP/C composite delivered an initial discharge capacity of  $93 \text{ mA h g}^{-1}$  at a current rate of  $0.05 \text{ C}$ ,<sup>22</sup> while the NVP/C composite fabricated by the sol-gel method delivered a reversible capacity of  $84.8 \text{ mA h g}^{-1}$  at a current density of  $0.2 \text{ C}$ .<sup>19</sup> Clearly, these values are much less than its theoretical capacity of  $117.6 \text{ mA h g}^{-1}$ .

It is of practical importance to develop a scalable method for mass production of a NVP/C composite which can maintain its superior electrochemical performance realized in lab-scale fabrication. Recently, our group has employed an aerosol based strategy to fabricate novel composite electrodes for sodium ion batteries.<sup>43</sup> The aerosol synthesis is a scalable production technique, and widely used in industry,<sup>44,45</sup> while the fabricated composite electrode demonstrates a porous and hollow structure. This one-step *in situ* formed robust structure with a carbon network surrounding the active particles provides a high contact area between electrode/electrolyte. These benefits have successfully contributed to the superior electrochemical performance of  $\text{Na}_2\text{FePO}_4\text{F/C}$  porous hollow spheres.<sup>43</sup>

In this work, we employ this aerosol based “droplets to particle” strategy to fabricate NVP/C porous hollow spheres through a modified ultrasonic spray pyrolysis device, which enables more favourable manifold production through the vertical design. By using the vertical device, the particle materials can be easily coated by carbon without agglomeration. The synthesis strategy of the NVP/C porous hollow spheres by the vertical ultrasonic spray pyrolysis reactor system is schematically illustrated in Scheme 1. The precursor solution of  $\text{NH}_4\text{H}_2\text{PO}_4$ ,  $\text{NH}_4\text{VO}_3$ ,  $\text{Na}_2\text{CO}_3$ , and citric acid was first pumped into an ultrasonic atomizer. Then the atomizer enables the spherical aerosol droplets with homogeneous composition with respect to the precursor solution, and disperses them inside the tube furnace *via* the Ar carrier gas. During the flow in the

furnace at  $600^\circ\text{C}$ , the surface layer of aerosol droplets will undergo solvent ( $\text{H}_2\text{O}$ ) evaporation, forming a solid shell consisting of solid citric acid spherical particles that uniformly encapsulate the stoichiometric composition of  $\text{NH}_4\text{H}_2\text{PO}_4$ ,  $\text{NH}_4\text{VO}_3$  and  $\text{Na}_2\text{CO}_3$  in the solid state, and further dehydration, decomposition, carbonization and chemical reactions to form hollow sphere particles. Citric acid in the precursor not only acts as the carbon source, but also as an *in situ* gas blowing agent to produce  $\text{CO}_2$  and  $\text{H}_2\text{O}$ . Together with the inherent gas generation properties of the  $\text{NH}_4\text{H}_2\text{PO}_4$ ,  $\text{NH}_4\text{VO}_3$  and  $\text{Na}_2\text{CO}_3$  salts, the gas blowing agents promote the formation of a hollow structure. The as-collected particles were further reacted, carbonized, and annealed at  $800^\circ\text{C}$  for 3 h under argon to obtain the crystalline NVP/C porous hollow spheres. As a cathode material of SIBs, these NVP/C porous hollow spheres exhibit one of the best electrochemical performances among the micron-sized NVP/C composites reported, especially when compared to the NVP/C composite prepared by the typical sol-gel method. This finding indicates that the aerosol method is an effective way to fabricate the  $\text{Na}_3\text{V}_2(\text{PO}_4)_3$  cathode material for practical application towards the mass production purpose.

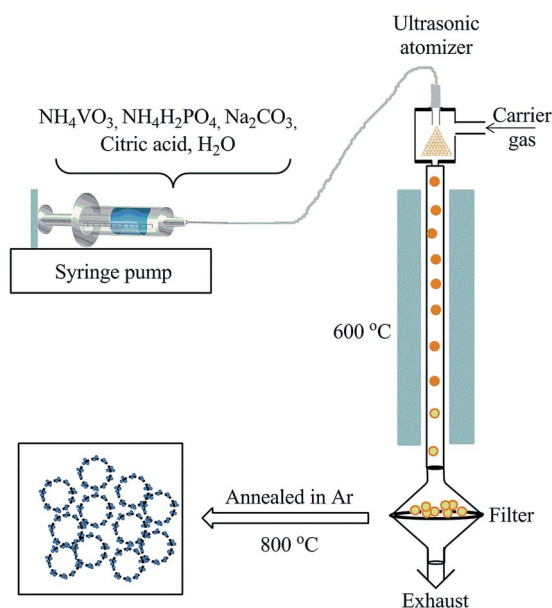
## Experimental

### Synthesis of the NVP/C electrode

The raw chemicals,  $\text{NH}_4\text{VO}_3$ ,  $\text{NH}_4\text{H}_2\text{PO}_4$ ,  $\text{Na}_2\text{CO}_3$ , and citric acid, were purchased from Sigma-Aldrich and used as received. The citric acid as a chelating agent and carbon source was dissolved in distilled water with continuous stirring at room temperature first. Then  $\text{NH}_4\text{VO}_3$ ,  $\text{NH}_4\text{H}_2\text{PO}_4$ , and  $\text{Na}_2\text{CO}_3$  in stoichiometric amounts were added into the solution in sequence under constant stirring. The obtained mixture was used as the precursor solution for further syntheses by aerosol and sol-gel methods. For the aerosol spray process, the precursor solution was loaded into a plastic syringe connected to a blunt-tip needle, which was connected to a syringe pump. The flow rate of the solution was set to be  $50 \mu\text{L min}^{-1}$ . The spray pyrolysis temperature was  $600^\circ\text{C}$ , while the argon carrier gas flow rate was held constant at 3 Lpm. Particles were collected on a polytetrafluoroethylene (PTFE) filter using a brush. The as-collected particles were then annealed at  $800^\circ\text{C}$  for 3 h under argon to obtain the crystalline NVP/C porous hollow spheres. For sol-gel methods, the precursor solution was continuously stirred and heated at  $80^\circ\text{C}$  to form a uniform solution. After evaporating the water for several hours with vigorous stirring, the solution transformed from sol to gel. After the transformation, the gel was dried in a vacuum oven at  $80^\circ\text{C}$  for at least 10 h. The obtained xerogel was ground in a mortar and heat-treated at  $300^\circ\text{C}$  in an argon atmosphere for 4 h. Then, the powders were ground again in a mortar and annealed at  $800^\circ\text{C}$  for 3 h under an argon atmosphere to obtain the final carbon coated NVP material.

### Material characterization

The crystal structure of the materials was characterized using powder X-ray diffraction (XRD) on a D8 Advanced facility



**Scheme 1** Schematic of the vertical ultrasonic spray pyrolysis process.

(Bruker AXS, WI, USA) using a CuK $\alpha$  radiation source. The morphology of the materials was characterized using both a Hitachi SU-70 analytical ultra-high-resolution scanning electron microscope (SEM) and JEM 2100 LaB6 emission transmission electron microscope (TEM) at the University of Maryland Nanoscale Imaging Spectroscopy and Properties Laboratory. The after-cycled electrode was rinsed with propylene carbonate (PC) before taking the images. Thermogravimetric analysis was performed on STA 449F3 equipment (Netzsch, Germany) at a heating rate of 10 °C min<sup>-1</sup> from room temperature to 600 °C in an air atmosphere to determine the carbon content in NVP/C composites. Raman measurements were performed on a Horiba JobinYvonLabramArakis Raman Spectrometer using a 532 nm diode-pumped solid-state laser, attenuated to give ~900  $\mu$ W power at the sample surface. The Brunauer–Emmett–Teller (BET) specific surface area and pore size and volume were analyzed using N<sub>2</sub> absorption with a Micromeritics ASAP 2020 Porosimeter Test Station.

### Electrochemical measurements

The NVP electrodes were prepared by the slurry coating method. The synthesized NVP/C composites were mixed with carbon black and a PVDF binder to form slurry at the weight ratio of 80 : 10 : 10. Then, the obtained slurry was cast on aluminium foil and dried in a vacuum oven at 100 °C overnight. Coin cells, consisting of a NVP working electrode, a sodium metal counter electrode, a Celgard 3501 separator, and 1.0 M NaClO<sub>4</sub> in ethylene carbonate/propylene carbonate/dimethyl carbonate (EC/PC/DMC, 0.45 : 0.45 : 0.1 v/v) co-solvent liquid electrolyte, were assembled in an argon-filled glove box for electrochemical tests.

Galvanostatic charge/discharge tests were performed on an Arbin battery test station (BT2000, Arbin Instruments, USA). The cells were cycled between 2.3 and 3.9 V under different current densities. Both the charge and discharge current density and specific capacity were calculated based on the overall mass of NVP/C composites in the electrode. Cyclic voltammetry (CV) testing at a scan rate of 0.1 mV s<sup>-1</sup> and impedance testing were conducted using a Gamry Potentiostat/Galvanostat/ZRA (Reference 3000, Gamry Instruments, USA).

## Results and discussion

The morphology of NVP/C prepared by aerosol and sol–gel methods is revealed by SEM and TEM images. The SEM images of the aerosol synthesized NVP/C composite after annealing under argon at 800 °C for 3 h are shown in Fig. 1a and b. Clearly, the aerosol NVP/C composite displays a typical spherical morphology. The size of the spheres ranges from 2 to 10  $\mu$ m. Moreover, a hollow structure with porous morphology can also be clearly observed. The wall is formed by sintering aggregated small particles thus leaving many cavities and nano- or micropores inside the wall. Meanwhile, the aerosol NVP/C composite shows a hierarchical structure, where the NVP particles (ranging from dozens to hundreds of nanometers) are uniformly attached to the outer and inner surfaces of the spherical carbon

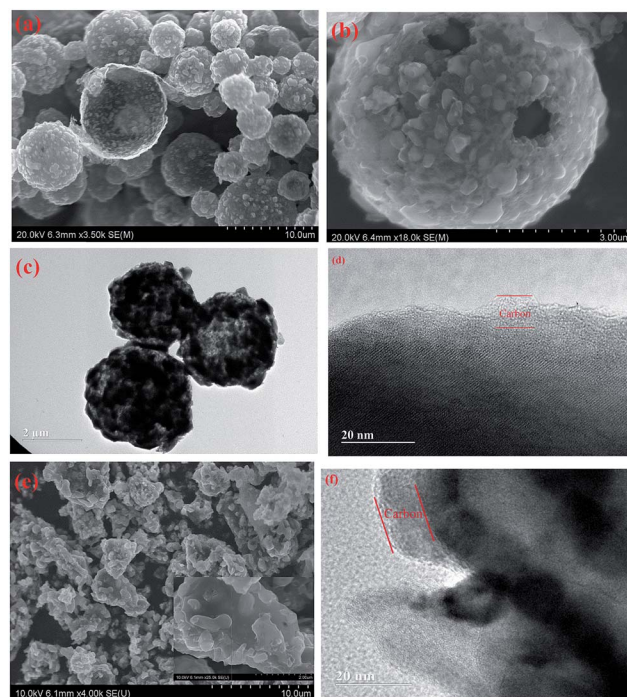


Fig. 1 (a and b) SEM image and (c and d) TEM image curves for the aerosol synthesized NVP/C composites, and (e) SEM images and (f) TEM images for the sol–gel synthesized NVP/C composites.

wall, which is confirmed by the TEM image (Fig. 1c). From the HRTEM image shown in Fig. 1d, a uniform amorphous carbon layer coated on the surface of NVP particles can be observed. In contrast, the sol–gel method synthesized NVP/C composite has an irregular shape morphology with the particle size ranging from 1 to 8  $\mu$ m (Fig. 1e). Also the sol–gel NVP/C composite shows obvious aggregation after annealing at 800 °C. The carbon coated layer on the sol–gel NVP/C composite is also confirmed by HRTEM (Fig. 1f).

The crystal structure of the NVP/C composites synthesized by aerosol and sol–gel methods was analyzed by X-ray diffraction (XRD), respectively, as shown in Fig. 2a. Both the NVP/C composites show the same peaks with similar peak positions, intensity ratios and peak sharpness. All of the diffraction peaks can be indexed to the standard pattern of Na<sub>3</sub>V<sub>2</sub>(PO<sub>4</sub>)<sub>3</sub> in the *R*3C space group. The nature and content of coated carbon in both the NVP/C composites were investigated using Raman measurements and thermogravimetric (TG) analyses. The Raman spectra of both the NVP/C composites are shown in Fig. 2b. Two Raman peaks at 1346 and 1597 cm<sup>-1</sup>, representing the disordered carbon (D band) and graphitized carbon (G band), respectively, are observed in both composites. The TG results (Fig. 2c) show that the carbon contents in the aerosol and sol–gel NVP/C composites are 7.5 wt% and 7.1 wt%, respectively. The pore size distribution and specific surface areas of both the NVP/C composites were characterized using the Brunauer–Emmett–Teller (BET) method (Fig. 2d). The BET surface area of the NVP/C porous hollow spheres is 55.5 m<sup>2</sup> g<sup>-1</sup>, which is clearly larger than that of the sol–gel NVP/C composite



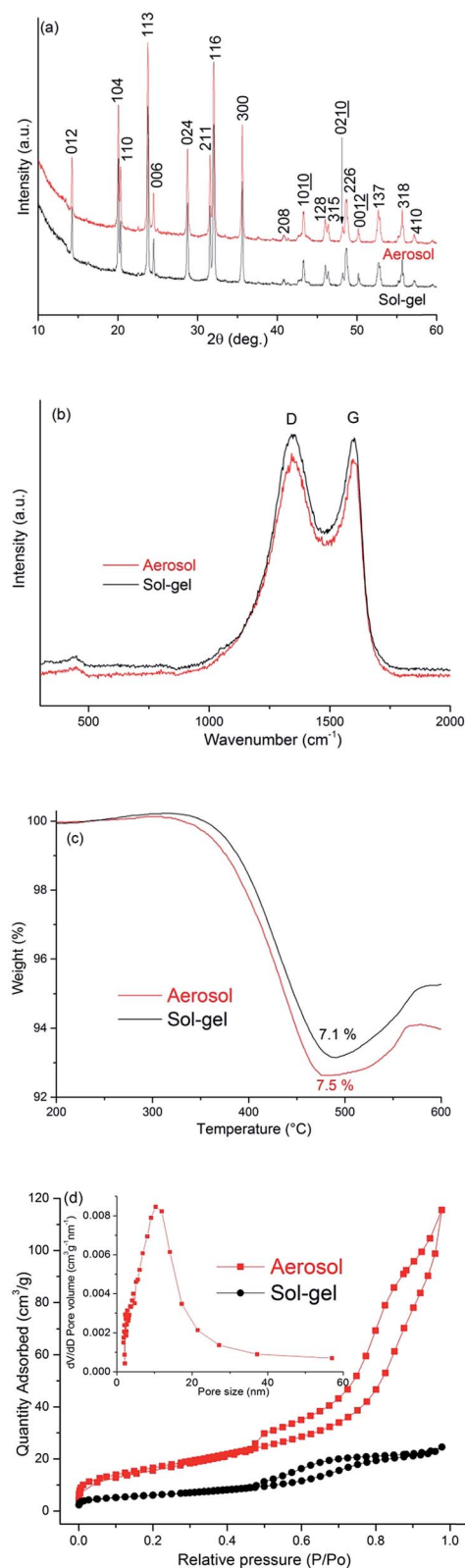


Fig. 2 (a) XRD patterns, (b) Raman spectra, (c) TG curves, and (d) N<sub>2</sub> adsorption/desorption isotherm for the aerosol and sol-gel method synthesized NVP/C composites, respectively; the inset of (d) is the BJH pore size distribution curve of the aerosol sample.

(21.0 m<sup>2</sup> g<sup>-1</sup>). This high surface area is mainly attributed to the hollow structure and the existence of pores generated by the accumulation of particles, just as observed in the SEM image (Fig. 1a and b). Moreover, the Barrett-Joyner-Halenda (BJH) desorption shows that the average pore size of NVP/C porous hollow spheres is around 11 nm. The pores in the wall will allow the liquid electrolyte to penetrate through the wall to the inside of the hollow sphere. Therefore, the electrochemical charge transfer reaction can take place on both sides of the wall and in the pores, thus leading to better Na<sup>+</sup> diffusion.

The sodiation/desodiation behavior of both the NVP/C samples was characterized using cyclic voltammetry (CV). Fig. 3a presents the cyclic voltammogram (CV) of the initial cycle for both samples at a scan rate of 0.1 mV s<sup>-1</sup> in the voltage range from 2.3 to 3.9 V. Clearly, one similar pair of oxidation (Na extraction) and corresponding reduction (Na insertion) peaks can be observed for these two samples, which are attributed to the V<sup>4+</sup>/V<sup>3+</sup> redox couple in the NVP material.<sup>18–42</sup> The voltage difference between oxidation and reduction peaks (0.26 V) for the aerosol NVP/C composite is smaller than that (0.35 V) of the sol-gel NVP/C composite. Such a small voltage hysteresis indicates the lower electrode polarization and hence probably leads to faster sodiation/desodiation kinetics.

Fig. 3b shows the charge/discharge curves of the aerosol sample at a current density of 20 mA g<sup>-1</sup> in the potential window of 2.3–3.9 V vs. Na<sup>+</sup>/Na. The voltage profiles show a pair of flat voltage plateaus during charge and discharge, demonstrating a reversible phase transformation between Na<sub>3</sub>V<sub>2</sub>(PO<sub>4</sub>)<sub>3</sub> and NaV<sub>2</sub>(PO<sub>4</sub>)<sub>3</sub>. The flat plateaus at about 3.4 V are consistent with the redox peaks in CV (Fig. 3a). Furthermore, the potential hysteresis between charge and discharge is only 0.04 V, further confirming the rapid reaction kinetics. The aerosol cathode delivers an initial charge capacity of 104 mA h g<sup>-1</sup> and a discharge capacity of 99.2 mA h g<sup>-1</sup>. Considering that there is 7.5 wt% of carbon in the composite, the capacity is very close to the theoretical capacity of NVP (117.6 mA h g<sup>-1</sup>). For comparison, the sol-gel sample was also investigated under the same conditions. As shown in Fig. 3c, the sol-gel sample displays similar charge/discharge profiles to the aerosol sample, but a larger potential hysteresis (0.07 V) at the same charge/discharge current is observed. The results are in good agreement with the CV that the aerosol cathode has much better sodiation/desodiation kinetics than the sol-gel cathode. Additionally, the sol-gel cathode delivers a higher initial charge capacity of 107 mA h g<sup>-1</sup>, but a lower discharge capacity of 97.4 mA h g<sup>-1</sup>. It indicates that the first cycle coulombic efficiency (91.0%) of the sol-gel sample is lower than that of the aerosol sample (95.4%).

The long term cycling stability of both samples at 20 mA g<sup>-1</sup> between 2.3 and 3.9 V versus Na<sup>+</sup>/Na is compared in Fig. 3d. Clearly, the aerosol cathode exhibits superior cycling stability to the sol-gel counterpart. The initial discharge capacity of the aerosol cathode is 99.2 mA h g<sup>-1</sup> and a reversible capacity of 89.3 mA h g<sup>-1</sup> is maintained after 300 charge/discharge cycles, corresponding to the capacity retention of 90%, and capacity decay of only 0.035% per cycle. The cycling stability of the aerosol NVP/C cathode is comparable to the cycling stability of commercial LIB cathodes.<sup>46</sup> In comparison, the discharge

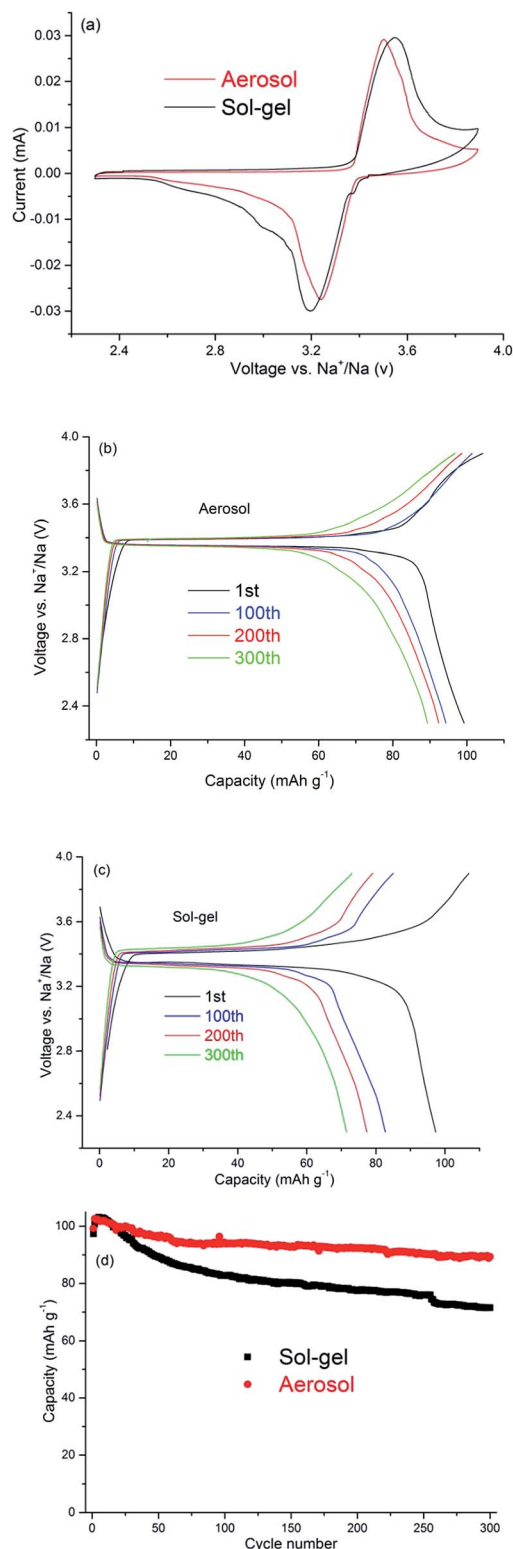


**Fig. 3** The electrochemical properties of aerosol and sol-gel synthesized NVP/C composites: (a) CV curves for both samples, (b) galvanostatic charge/discharge curves of aerosol NVP/C composites for the 1<sup>st</sup>, 100<sup>th</sup>, 200<sup>th</sup>, and 300<sup>th</sup> cycles at 20 mA g<sup>-1</sup>, (c) galvanostatic charge/discharge curves of sol-gel NVP/C composites for the 1<sup>st</sup>, 100<sup>th</sup>, 200<sup>th</sup>, and 300<sup>th</sup> cycles at 20 mA g<sup>-1</sup>, and (d) comparison of the cycling performances at 20 mA g<sup>-1</sup> for the both samples. All of the tests were performed in the potential window of 2.3–3.9 V (vs. Na<sup>+</sup>/Na).

capacity of the sol-gel cathode decreases from 97.4 to 71.5 mA h g<sup>-1</sup> after 300 cycles with a low capacity retention of 73.4%, displaying the poor cycling performance.

The advantages of the aerosol NVP/C composite were also evidenced by the rate performance at various current densities (ranging from 20 to 1000 mA g<sup>-1</sup>). Fig. 4a shows the rate capability of both samples. Obviously, the aerosol cathode has better rate performance than the sol-gel cathode. Both samples deliver a similar discharge capacity of around 100 mA h g<sup>-1</sup> at a low rate of 20 mA g<sup>-1</sup> in the first several cycles. However, the performance diverges at larger current densities. The aerosol cathode delivers the discharge capacities of 93.5, 84.9, 75.8, 29.5, and 9.6 mA h g<sup>-1</sup> at 50, 100, 200, 500 and 1000 mA g<sup>-1</sup>, respectively, whereas the sol-gel cathode delivers the discharge capacities of 88.6, 82, 70.5, 12.8, and 3.9 mA h g<sup>-1</sup>, respectively, at the same current densities. Obviously, the aerosol cathode delivers higher capacities than that of the sol-gel cathode at elevated current densities. When the current decreases back to 20 mA g<sup>-1</sup>, the discharging capacity of the aerosol cathode recovers to 94.5 mA h g<sup>-1</sup>, which is higher than that of the sol-gel cathode (86.1 mA h g<sup>-1</sup>), demonstrating a robust tolerance to current change of the aerosol cathode.

To better understand the superior cycling performance of the aerosol cathode, electrochemical impedance spectroscopy (EIS) measurement was performed for both aerosol and sol-gel fresh electrodes. The Nyquist plots and the equivalent circuit are presented in Fig. 4b. The EIS curves are composed of a depressed semicircle in the high frequency region, and a straight sloping line in the low frequency region. The resistor  $R_{ct}$  paralleled with the constant phase element (CPE) are the charge-transfer resistances at the electrode/electrolyte interface between the electrolyte and the cathode, which are assigned to the depressed semicircle.<sup>26,35</sup> By comparing the charge transfer resistance ( $R_{ct}$ ), it is found that the  $R_{ct}$  of the aerosol cathode (264.5 Ohm) is lower than that of the sol-gel cathode (310.8 Ohm). The higher the charge-transfer resistance, the slower the kinetics of the cell reactions.  $Z_w$  reflects the Warburg impedance related to the diffusion of Na<sup>+</sup> within the electrode, which is indicated by a straight sloping line. The Na<sup>+</sup> diffusion coefficient ( $D$ ) can be calculated using the equation  $D = R^2 T^2 / 2A^2 n^4 F^4 C^2 \sigma^2$ , where  $R$  is the gas constant,  $T$  is the temperature,  $A$  is the area of the electrode surface,  $n$  is the number of electrons per molecule during oxidation,  $F$  is the Faraday constant,  $\sigma$  is the Warburg factor, and  $C$  is the molar concentration of Na<sup>+</sup>.<sup>25,26,35</sup> The calculated sodium diffusion coefficient values for the aerosol and sol-gel cathodes are  $2.79 \times 10^{-16}$  and  $2.35 \times 10^{-16}$  cm<sup>2</sup> s<sup>-1</sup>, respectively. It can be found that the sodium diffusion coefficient of the aerosol cathode possesses a higher value than that of the sol-gel cathode, indicating the faster Na<sup>+</sup> transport in the aerosol cathode.

To explore the reasons for the exceptional battery performance of the aerosol cathode, the morphology after long-term cycling is studied by the post-cycling SEM and EDS analyses. Fig. 5 shows the SEM and EDS mapping images of the aerosol cathode after 300 charge/discharge cycles. Some of the spherical morphologies are well maintained after cycling, suggesting the structural stability and the architectural merit. The uniform

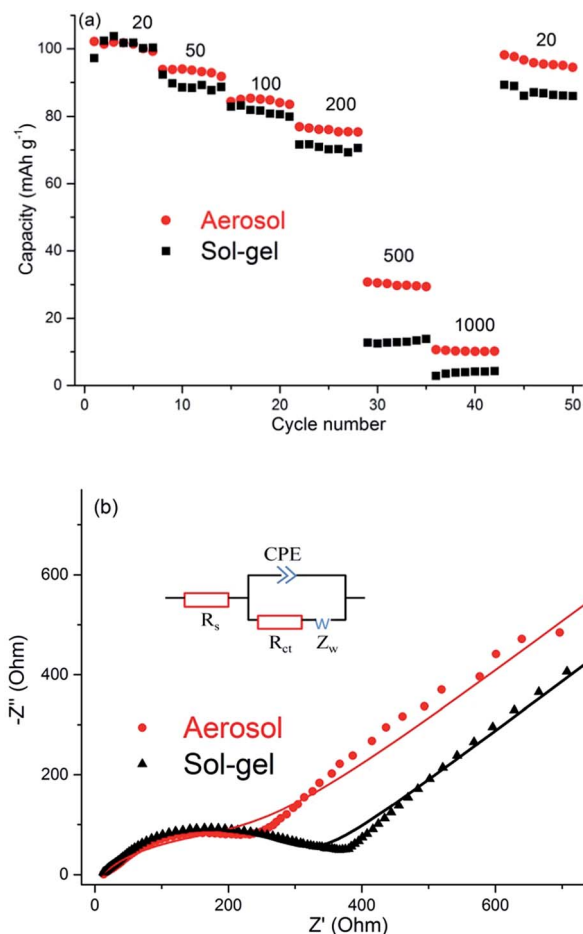


Fig. 4 (a) Rate capabilities for both aerosol and sol-gel samples at the varied current rates of 20–1000 mA g<sup>-1</sup>. (b) Electrochemical impedance spectra of both aerosol and sol-gel electrodes. The solid lines are the fitting curve by using the equivalent circuit which is shown as the inset and consists of a resistor ( $R_s$ ) and a constant phase element (CPE) parallel with a resistor ( $R_{ct}$ ) which is connected with a Warburg element ( $Z_w$ ) in series.

distribution of Na, P, V, and C in the NVP/C particles demonstrates the good morphology maintenance of NVP in the carbon matrix after long-term cycling. However, it should be noted that some of the spherical structures may still be damaged. The superior electrochemical performance of the aerosol cathode could be attributed to the hollow structure and spherical morphology, which could accommodate the volume change during sodiation/desodiation, and hence retain the good structural stability during long-cycling.

Basically, the NVP/C porous hollow spheres synthesized by the aerosol process demonstrated an excellent rate capability and cycling stability in NIBs, especially when compared to the NVP/C composite synthesized by the sol-gel method. Furthermore, the electrochemical performance of the aerosol NVP/C cathode is the best among all micron-sized NVP/C composites reported to date.<sup>18–22</sup> Particularly, the carbon content in the aerosol NVP/C cathode (including the carbon black) at 16 wt% is quite low.<sup>18–40</sup> In contrast, a high carbon content (>20 wt%) is

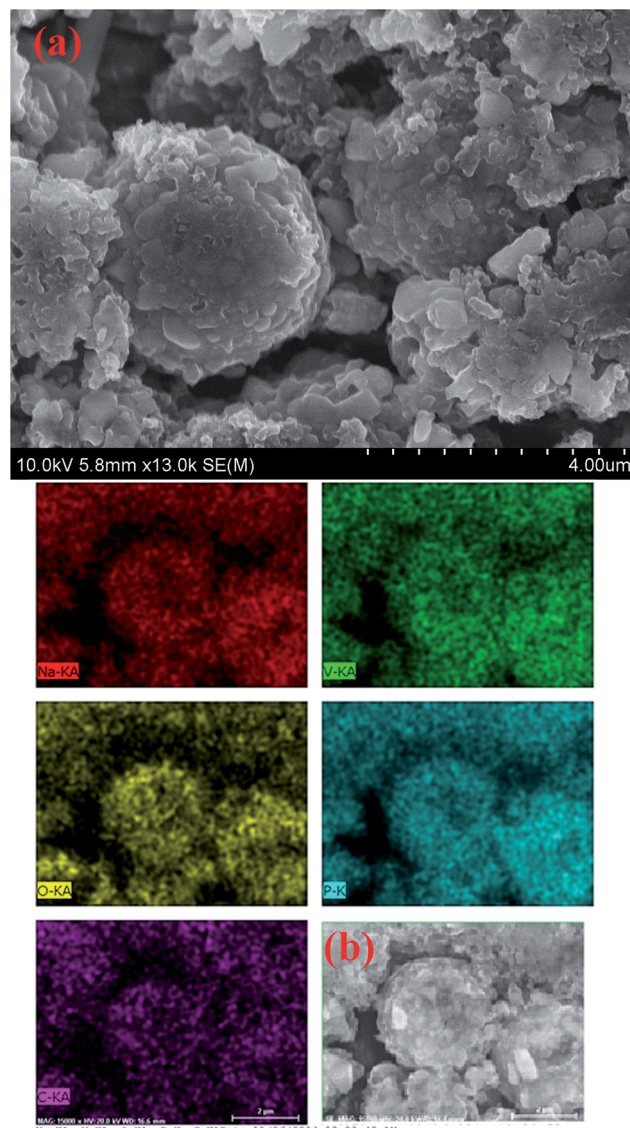


Fig. 5 (a) SEM images and (b) EDS element mapping images of the aerosol electrode after 300 charge/discharge cycles.

used in most NVP/C nanocomposites.<sup>22–40</sup> The superior performance of NVP/C porous hollow spheres can be attributed to their unique structure and morphology. The high surface area of the porous hollow structure enables a large contact area between the electrolyte and the electrode, and hence facilitates the electrochemical reactions. The hollow carbon matrices as a conductive network, as well as the carbon coating, could provide the continuous electron transport and better contact with the electrolyte, hence improving the electronic conductivity and increasing the reaction kinetics. Therefore, the shorter intercalation distance for Na<sup>+</sup> and the better conductive pathways for electrons in the NVP/C porous hollow spheres result in the good electrochemical performance. Moreover, the hollow spheres provide the robustness to accommodate the volume change and alleviate the stress and strain during Na<sup>+</sup> insertion/extraction, and thus improve the cycling stability.



Furthermore, we have shown that a scalable aerosol spray pyrolysis method can be used to create hierarchical NVP/C composites, where the carbon coated NVP is uniformly distributed in the inner and outer surfaces of the porous hollow carbon matrix. The aerosol process is easy to operate and control, and is feasible for large-scale production of the composite. By optimizing the composition of the precursors (e.g. tuning the amount of citric acid, or using different chelating agents or carbon sources) and the operating conditions for the spray pyrolysis process (e.g. temperature, flow rate, or length of the tube furnace), the structure, morphology, and the particle size could be tuned to further improve the electrochemical performance.

## Conclusions

In summary, we successfully synthesized the unique porous hollow carbon spheres with uniformly attached carbon coated  $\text{Na}_3\text{V}_2(\text{PO}_4)_3$  particles by using a vertical ultrasonic spray pyrolysis technique. The synthesis process is easy to operate and control, and is feasible for large-scale production of the composite cathode or anode materials. The as-prepared NVP/C porous hollow spheres exhibited excellent electrochemical performance as a cathode material for SIBs. A specific discharge capacity of  $99.2 \text{ mA h g}^{-1}$  (total weight of NVP and C) at  $20 \text{ mA g}^{-1}$  is achieved in the first cycle, and 90% of the initial capacity is retained after 300 charge/discharge cycles. The enhanced electrochemical performance is ascribed to its unique structure, hollow spherical and porous morphology, and carbon-coating layer.

## Acknowledgements

The research post for JM has received funding from the DOE ARPA-E (DEAR0000389). The support from the Maryland NanoCenter and its NispLab is also acknowledged.

## Notes and references

- 1 B. Dunn, H. Kamath and J. M. Tarascon, *Science*, 2011, **334**, 928.
- 2 M. D. Slater, D. Kim, E. Lee and C. S. Johnson, *Adv. Funct. Mater.*, 2013, **23**, 947.
- 3 V. Palomares, P. Serras, I. Villaluenga, K. B. Hueso, J. Carretero-Gonzalez and T. Rojo, *Energy Environ. Sci.*, 2012, **5**, 5884.
- 4 H. L. Pan, Y. S. Hu and L. Q. Chen, *Energy Environ. Sci.*, 2013, **6**, 2338.
- 5 N. Yabuuchi, K. Kubota, M. Dahbi and S. Komaba, *Chem. Rev.*, 2014, **114**, 11636.
- 6 M. H. Han, E. Gonzalo, G. Singh and T. Rojo, *Energy Environ. Sci.*, 2015, **8**, 81.
- 7 R. Berthelot, D. Carlier and C. Delmas, *Nat. Mater.*, 2011, **10**, 74.
- 8 J. Billaud, R. J. Clément, A. R. Armstrong, J. Canales-Vázquez, P. Rozier, C. P. Grey and P. G. Bruce, *J. Am. Chem. Soc.*, 2014, **136**, 17243.
- 9 N. Yabuuchi, H. Yoshida and S. Komaba, *Electrochemistry*, 2012, **80**, 716–719.
- 10 N. Yabuuchi, M. Kajiyama, J. Iwatate, H. Nishikawa, S. Hitomi, R. Okuyama, R. Usui, Y. Yamada and S. Komaba, *Nat. Mater.*, 2012, **11**, 512.
- 11 P. Moreau, D. Guyomard, J. Gaubicher and F. Boucher, *Chem. Mater.*, 2010, **22**, 4126.
- 12 Y. J. Zhu, Y. H. Xu, Y. H. Liu, C. Luo and C. S. Wang, *Nanoscale*, 2013, **5**, 780.
- 13 K. T. Lee, T. N. Ramesh, F. Nan, G. Botton and L. F. Nazar, *Chem. Mater.*, 2011, **23**, 3593.
- 14 P. Barpanda, J.-N. Chotard, N. Recham, C. Delacourt, M. Ati, L. Dupont, M. Armand and J.-M. Tarascon, *Inorg. Chem.*, 2010, **49**, 7401.
- 15 P. Barpanda, G. Oyama, S. Nishimura, S. C. Chung and A. Yamada, *Nat. Commun.*, 2014, **5**, 4358.
- 16 P. Senguttuvan, G. Rousse, M. E. Arroyo y de Dompablo, H. Vezin, J. M. Tarascon and M. R. Palacin, *J. Am. Chem. Soc.*, 2013, **135**, 3897.
- 17 Y. Uebou, T. Kiyabu, S. Okada and J. Yamaki, *Rep. Inst. Adv. Mater. Study*, 2002, **16**, 1.
- 18 M. Pivko, I. Arcon, M. Bele, R. Dominko and M. Gaberscek, *J. Power Sources*, 2012, **216**, 145.
- 19 S. Y. Lim, H. Kim, R. A. Shakoob, Y. Jung and J. W. Choi, *J. Electrochem. Soc.*, 2012, **159**, A1393.
- 20 W. X. Song, X. B. Ji, Z. P. Wu, Y. N. Zhu, Y. C. Yang, J. Chen, M. J. Jing, F. Q. Li and C. E. Banks, *J. Mater. Chem. A*, 2014, **2**, 5358.
- 21 Z. L. Jian, C. C. Yuan, W. Z. Han, X. Lu, L. Gu, X. K. Xi, Y. S. Hu, H. Li, W. Chen, D. F. Chen, Y. Ikuhara and L. Q. Chen, *Adv. Funct. Mater.*, 2014, **24**, 4265.
- 22 Z. L. Jian, L. Zhao, H. L. Pan, Y. S. Hu, H. Li, W. Chen and L. Q. Chen, *Electrochem. Commun.*, 2012, **14**, 86.
- 23 Z. L. Jian, W. Z. Han, X. Lu, H. X. Yang, Y. S. Hu, J. Zhou, Z. B. Zhou, J. Q. Li, W. Chen, D. F. Chen and L. Q. Chen, *Adv. Energy Mater.*, 2013, **3**, 156.
- 24 K. Saravanan, C. W. Mason, A. Rudola, K. H. Wong and P. Balaya, *Adv. Energy Mater.*, 2013, **3**, 444.
- 25 W. C. Duan, Z. Q. Zhu, H. Li, Z. Hu, K. Zhang, F. Y. Cheng and J. Chen, *J. Mater. Chem. A*, 2014, **2**, 8668.
- 26 J. Liu, K. Tang, K. P. Song, P. A. van Aken, Y. Yu and J. Maier, *Nanoscale*, 2014, **6**, 5081.
- 27 Y. Jiang, Z. Z. Yang, W. H. Li, L. C. Zeng, F. S. Pan, M. Wang, X. Wei, G. T. Hu, L. Gu, and Y. Yu, 2015, DOI: 10.1002/aenm.201402104.
- 28 Q. Y. Wang, B. D. Zhao, S. Zhang, X. H. Gao and C. Deng, *J. Mater. Chem. A*, 2015, **3**, 7732.
- 29 M. J. Aragón, P. Lavelaz, G. F. Ortiz and J. L. Tirado, *J. Electrochem. Soc.*, 2015, **162**, A3077.
- 30 H. Wang, D. L. Jiang, Y. Zhang, G. P. Li, X. Z. Lan, H. H. Zhong, Z. P. Zhang and Y. Jiang, *Electrochim. Acta*, 2015, **155**, 23.
- 31 W. Shen, C. Wang, Q. J. Xu, H. M. Liu and Y. G. Wang, *Adv. Energy Mater.*, 2014, **5**, 1400982.
- 32 W. Shen, C. Wang, H. M. Liu and W. S. Yang, *Chem.-Eur. J.*, 2013, **19**, 14712.

- 33 Y. H. Jung, C. H. Lim and D. K. Kim, *J. Mater. Chem. A*, 2013, **1**, 11350.
- 34 J. Kang, S. Baek, V. Mathew, J. Gim, J. J. Song, H. Park, E. Chae, A. K. Rai and J. Kim, *J. Mater. Chem.*, 2012, **22**, 20857.
- 35 S. Li, Y. F. Dong, L. Xu, X. Xu, L. He and L. Q. Mai, *Adv. Mater.*, 2014, **26**, 3545.
- 36 C. B. Zhu, K. P. Song, P. A. van Aken, J. Maier and Y. Yu, *Nano Lett.*, 2014, **14**, 2175.
- 37 S. Kajiyama, J. Kikkawa, J. Hoshino, M. Okubo and E. Hosono, *Chem.–Eur. J.*, 2014, **20**, 12636.
- 38 H. Li, Y. Bai, F. Wu, Y. Li and C. Wu, *J. Power Sources*, 2015, **273**, 784.
- 39 G. Q. Li, D. L. Jiang, H. Wang, X. Z. Lan, H. H. Zhong and Y. Jiang, *J. Power Sources*, 2014, **265**, 325.
- 40 P. Nie, Y. Y. Zhu, L. F. Shen, G. Pang, G. Y. Xu, S. Y. Dong, H. Dou and X. G. Zhang, *J. Mater. Chem. A*, 2014, **2**, 18606.
- 41 J. H. Yang, D. W. Han, M. R. Jo, K. Song, Y. Kim, S. L. Chou, H. K. Liu and Y. M. Kang, *J. Mater. Chem. A*, 2015, **3**, 1005.
- 42 S. J. Lim, D. W. Han, D. H. Nam, K. S. Hong, J. Y. Eom, W. H. Ryu and H. S. Kwon, *J. Mater. Chem. A*, 2014, **2**, 19623.
- 43 A. Langrock, Y. H. Xu, Y. H. Liu, S. Ehrman, A. Manivannan and C. S. Wang, *J. Power Sources*, 2013, **223**, 62.
- 44 A. B. D. Nandiyanto and K. Okuyama, *Adv. Powder Technol.*, 2011, **22**, 1.
- 45 D. S. Jung, Y. N. Ko, Y. C. Kang and S. B. Park, *Adv. Powder Technol.*, 2014, **25**, 18.
- 46 K. Ozawa, *Solid State Ionics*, 1994, **69**, 212.